CLM-P719

CLM-P719

UKAEA

Preprint

THE TOMOGRAPHY OF NEUTRAL BEAMS

G. A. COTTRELL

CULHAM LABORATORY
Abingdon Oxfordshire
1984

CLM-P719

THE TOMOGRAPHY OF NEUTRAL BEAMS

G.A. Cottrell

Culham Laboratory, Abingdon, Oxon., OX14 3DB, UK

(Euratom/UKAEA Fusion Association)

Abstract

This paper describes a new diagnostic technique to decode information contained in the spectral and spatial distribution of photons emitted by fast neutral beam particles and provide an estimate of the 2D beam density distribution function in a cross-sectional slice. By scanning Doppler-shifted Hα radiation from the fast beam particles at a number of peripheral locations around the beam axis, tomographic reconstructions of the beam distribution with spatial resolution $\Delta x \simeq 2$cm and time resolution $\Delta t \simeq 10$ms can be made. Using a Maximum Entropy reconstruction algorithm (making no symmetry assumptions), experimental reconstructions are presented of the 2D profile of the beam produced by the prototype JET source for each of the Doppler-shifted line radiation components.

(Submitted for publication in Review of Scientific Instruments)

March 1984

1. INTRODUCTION

Recent developments in neutral hydrogen (or deuterium) atom injectors, for use in controlled thermonuclear research, have led to the production of particle beams of high brightness. However, beam power density and pulse lengths have now increased to levels where it is no longer possible to determine the transport properties of the beam using material probes. For example, in the JET PINI (Plug In Neutral Injector) modular ion source[1], a 5MW (E_b = 80keV per nucleon, I = 60A extracted current) ion beam is pulsed for 5s. At the centre of the beam the peak power density is $\lesssim$ 30kW cm^{-2} which can exceed the safe operating limits on actively cooled probes for these long pulse times. However it remains important to be able to diagnose beams as fully as possible on developmental test stands where beam performance can be evaluated.

Attention has therefore been directed here to exploiting non-intrusive diagnostic methods; one powerful technique is to analyse the beam light emitted by the fast particles. This radiation originates from collisions of the fast particles with background H_2 (or D_2) molecules in the flight chamber resulting in fast, excited atoms which can decay by photon emission. A considerable amount of beam information is coded in both the spectral and spatial components of the emitted photon distribution. Optical Doppler shift spectroscopic measurements can, for example allow the discrimination of the radiation from the different energetic beam species whereas angularly resolved optical measurements can allow estimates to be made of the beam distribution in space.

This paper shows how, by combining spatial and spectral measurements of the distribution of photons, sufficient data can be collected to allow tomographic reconstruction of the two dimensional beam density distribution function f(x,y) (in a cross sectional slice) for each of the energetic species independently. Knowledge of f(x,y) can then allow estimates to be made of beam transmission (through limited sized ducts), power density levels and beam focussing quality[8]. Beam transmission depends on both the beamlet divergence and the steering of the beamlet array. The mixed ion and neutral beam fractions emerging from the exit of the gas neutraliser cell in a positive ion based injector contain three main energy components. The plasma source produces H^+, H_2^+ and H_3^+ ions which are extracted with energy, E; the H_2^+ and H_3^+ ions are subsequently collisionally dissociated after passage through a thick gas target. The emergent beam predominantly contains H^+ and H_0 particles with energies of E, E/2 and E/3. Radiation for each of these neutral species can be separated experimentally using the technique of Doppler-shift spectroscopy.

2. OPTICAL BEAM DIAGNOSIS

Line radiation from the fast particles is emitted in two collisional reactions with the background molecules:

i) Charge-exchange excitation collisions

$$\underline{H}^+ + H_2 \rightarrow \underline{H}_0^* + [H_2] \rightarrow \text{photon} \qquad \ldots (1)$$

ii) Excitation of ground state neutrals

$$\underline{H}^o + H2 \rightarrow \underline{H}_0^* + [H2] \rightarrow \text{photon}. \qquad \ldots (2)$$

Here, the underlined symbol denotes a fast particle and the asterisk an excited neutral (n = 3 for Hα radiation). The square brackets denote the possibility of dissociation of the background gas molecules. Cross-sections for both of these reactions have been measured recently for Balmer Alpha radiation[2]; using these it is useful to compute the fraction of Hα light from process i), $\varepsilon_+/(\varepsilon_+ + \varepsilon_o)$, where ε_+ and ε_o are the relative Hα emissivities of the ions and neutrals. The energy dependence of this function is shown in Fig. 1 for the case of a highly equilibrated beam of protons (gas target thickness $\pi = 1 \times 10^{16}$ H_2 molecules/cm^2). These data show that, for extracted beams of 60-80 keV, ≃ 65% of the Hα emission from the full energy particles comes from ion charge-exchange whereas, for E/2 and E/3 particles, the dominant Hα radiation comes from neutral impact excitation and decay. We next consider what information can be extracted from various kinds of measurements of this radiation.

2.1 Doppler Shift Spectroscopy

Doppler-shifted Hα emission from the full and fractional energy particles can be separated by making spectrally resolved measurements, usually along a central chord intersecting the beam[3, 4, 5]. A typical spectrum is shown in Fig. 2. Essentially two kinds of information can be obtained from such spectra. First, the relative fluxes (H^+:H_2^+:H_3^+) of the extracted ions may be derived from the ratios of the line areas with a knowledge of the cross-section of processes (1) and (2). Second, information on the transverse beam velocity dispersion can be obtained from the Doppler-broadening of the lines. However, deconvolution of the line broadening into components due to beamlet angular divergence and beamlet array steering is difficult, particularly when the emitted spectral lines are distorted

significantly by the spectrometer instrumental point spread function and when noise is present on the data.

2.2 The Flying Spot Scanner

Both parallel and fan-beam projections of the Hα beam light have previously been measured using either an array of detectors[6] or rotating mirror scanner[7]. The fan-beam projection data were optically filtered (using a Fabry-Perot etalon) to provide spectral discrimination of the beam species. A fan-beam projection is geometrically equivalent to a pinhole 'image' of the beam in a cross-sectional slice. Because the pinhole image of the beam is constructed from a set of equally spaced angular line integral averages, only information on the projection of $f(x,y)$ can be obtained.

One approach to the interpretation of single scanner data has been to fit an empirical (three dimensional) model of the beam seen in projection. For this, free model parameters such as beamlet divergence and focal length can be used. One 3D model used[8] assumed the summation of a number of steered Gaussian point-beamlet-emitters, arranged in positions corresponding to apertures in a multi-hole extraction system; the beam particle densities were calculated assuming straight-line particle trajectories. Implicit in this model was also the assumption of bi-axial symmetry (for the case of a rectangular extraction system) with two different focal lengths in each principal transport plane. Experimentally, several orthogonal pairs of scanners were used[8] to sample Hα light projection data from a number of different axial positions and orientations. The fit of an empirical model to such data can allow the combined effects of beamlet divergence and steering to be evaluated separately. However, in practice, even with data from several scanners there are problems in determining whether or not the

model fit is unique or if the boundary conditions have been correctly specified. If, for example, non-linear differential beamlet steering effects were present it would be difficult to determine their magnitude. Moreover, in a mixed ion and neutral beam the trajectories of the ions are susceptible to any uncompensated space-charge forces[9], external and self magnetic fields[10] or by extraneous electromagnetic fields; such effects would clearly invalidate the assumption of straight-line ion trajectories used in the model.

These considerations have led us to seek a model-independent way of analysing beam projection data. The alternative presented here is to use the data to reconstruct a 2D picture of the beam density distribution (tomograph) making no a priori assumptions about the beam shape. Such data can assist in forming a consistent picture of the transport of the particle beam.

3. NEUTRAL BEAM TOMOGRAPHY

3.1 The General Problem of Tomography

The particle beam is assumed to be viewed by a number of fan-beam scanners (Fig. 3). The unknown two-dimensional neutral beam emissivity function, $f(x,y)$, is projected along the viewing lines shown giving a signal response at detector k ($k = 1,M$)

$$d_k = \iint g_k(\phi)\, r^{-1}\, f(x,y)\, dx\, dy \qquad \ldots (3)$$

where g_K, the angular response function of the detector, is assumed to be given by

$$g_k(\phi) = A \exp[-(\phi - \phi_o)^2/\Delta\phi^2]. \quad \ldots (4)$$

Here, ϕ is the angle of incoming light rays with respect to the instantaneous pointing angle of the scanner (ϕ_o), $\Delta\phi$ is the halfwidth angle at 1/e of the maximum and A a constant.

The fundamental problem in tomography is to invert eq.(3), and evaluate the function $f(x,y)$ from the data d_k. An approximation to eq.(3) can be obtained by representing $f(x,y)$ by a discrete set of values $\{f_j\}$ ($j = 1,N$) and calculating the matrix element contributions O_{jk} from the jth pixel (picture element) to detector k using eq.(4). This system is represented by the set of equations

$$d_k = O_{jk} f_j + n_k \quad \ldots (5)$$

where n_k is the noise on datum k. In the high signal-to-noise ratio limit $n_k = 0$ and if sufficient views of the object are available to reconstruct the object uniquely to a given bandwidth one can solve eq.(5) by linear inversion

$$f_j = O^{-1}_{jk} d_k, \quad \ldots (6)$$

which clearly shows the inverse nature of the problem. However in the present application (as in many plasma physics experiments) the line integral data are both sparse and noisy. In this situation, one has to seek suitable solution techniques.

3.2 The Sparse Data Problem

It was shown by Radon[11] that $f(x,y)$ cannot be determined completely if the number of projections is finite; in this case the object must be bandwidth limited. The Central Slice theorem[12] can be used to determine the information available in a reconstruction when only a few projections are available. The theorem states that, for parallel projections, the Fourier transform of a projection at angle γ is equal to the Fourier transform of the object evaluated along the line at angle γ passing through the origin. Thus to reconstruct an object with diameter D showing structure on finest scale Δx, we need

$$n = \frac{\pi D}{\Delta x} \qquad \ldots (7)$$

projections[13] (assuming the projections to be continuous). For projection data sampled according to the Nyquist criterion there must be 2 samples per cycle of the highest spatial frequency. Thus of order $2D/\Delta x$ samples per projection are needed.

In the neutral beam tomography method described it is desirable to use the maximum available scanner camera resolution ($\Delta\phi = 0.5^0$, equivalent to $\Delta x = \Delta y \simeq 2$ cm in the centre of the beam). The beam profile was reconstructed in a circular region of diameter D = 72 cm. For this geometry and required resolution $n \simeq 100$ cameras are needed, a large number of cameras to operate on a beamline. However, engineering constraints limit the maximum practical number to $n \simeq 12$. Because of this constraint, an interpolation scheme must be chosen to fill in the unmeasured regions of Fourier space. Several interpolation methods have been investigated[14,15,16]. In the case of linear reconstruction

methods for example, filtered back-projection, reasonable results can be obtained for objects with some circular symmetry but prominent artifacts can arise on objects with oriented structure.

3.3 Maximum Entropy Method

In this paper, we pursue the non-linear Maximum Entropy (ME) method of obtaining the solution. This has been described briefly earlier[20]. From the set of reconstructions whose projections agree with the known projection data (within its errors), a representative member is selected to be displayed. In this case, the representative member is the (positive-valued) reconstruction having the maximum configurational entropy, S, where

$$S = - \sum p_j \log p_j \qquad \ldots (8)$$

and

$$p_j = \frac{f_j}{\sum f_j} .$$

The entropy, S, is a measure of missing information[17]; thus the ME reconstruction contains the least amount of global structure, yet it is still consistent with the known projection data. This (unique) reconstruction therefore contains the minimum of spurious structure, artefacts and noise; only such information or image structure as is required to fit the data is present.

Consistency of the ME solution with the projection data is obtained via the χ^2 statistic:

$$\chi^2 = \sum_k (O_{jk} f_j - d_k)^2/\sigma_k^2 \qquad \ldots (9)$$
$$= M + 3.29 \sqrt{M}$$

where σ_k is the uncertainty in d_k. This value of χ^2 corresponds to the 99 percent confidence level; one can therefore be 99 percent certain

that the true object contains at least as much structure as that contained in the ME reconstruction. Since S is undefined for $f_j \leq 0$ the ME solution is always non-negative. Physical objects viewed via projections of their emission (or absorption) relative to a zero background must indeed be positive. Thus the ME solution has the advantage of containing no (unphysical) negative regions, of the type often produced by analytic Fourier reconstruction methods[18].

The constrained maximisation of the entropy was performed iteratively[19]. Initially, the $\{f_j\}$ were set equal; this map is the unconstrained ME solution which contains no structural information. The algorithm then iterates $\{f_j\}$ towards the target solution working in a three-dimensional subspace of search directions related to current values of $-\nabla\chi^2$ (to fit the data) and ∇S (to increase the entropy). During iteration the normalised χ^2 statistic decreases monotonically towards its target value $\chi^2/N = 1$. This procedure can be illustrated by considering the two dimensional ($\{f\} = \{f_1, f_2\}$) phase-space diagram (Fig. 4). The starting point for the algorithm is the unconstrained ME solution ($f_1 = f_2$); successive iterates move the vector in the direction shown on the figure. Iteration is stopped when the value of the normalised chi-squared equals unity giving the constrained ME solution. In the application described here the solution is found in a 4096-dimensional space. The algorithm was checked frequently for correct convergence by calculating the angle between the vectors $\nabla\chi^2$ and ∇S; these vectors are parallel at the unique ME solution.

The development of the solution in the 4096-dimension tomographic problem is illustrated in Fig. 5 after 1,3,5 and 15 iterations. Beyond this number of iterations no significant changes occurred to the solution (the normalised value of $\chi^2/N = 1.0$ after the 15th iteration).

This example was constructed from trial sparse beam profile data[7] using just seven cameras (at positions C_1, C_2, C_3, C_4, C_6, C_8 and C_{12} on Fig. 3). The main computational effort was needed to calculate the search directions; this required six transformations between map and data space per iteration. The computer time for reconstructions of the size in this example (using a 64 x 64 point mesh) was approximately one minute on an ICL 2976 mainframe computer.

4. EXPERIMENTAL BEAM TOMOGRAPHY SYSTEM

A numerical study has been performed[20] to evaluate the reconstruction quality in cases where only a limited number of scanning cameras are available and used in the design of a practical apparatus. The procedure adopted was as follows.

(i) Calculate a two-dimensional simulated neutral beam density profile.

(ii) Calculate the projected light profile at each camera station.

(iii) Add noise to the projection data to simulate real observations.

(iv) Use the ME algorithm to reconstruct the two-dimensional beam distribution.

(v) Compare the result of (iv) with that of (i).

Trials were performed using different numbers of cameras, different neutral beam parameters and shapes as well as with different quantities of noise added to the projection data. Results showed that with as few as 12 cameras arranged symmetrically around the beam, it could be reconstructed accurately for map intensities $\gtrsim$ 1% of the maximum. This level of reconstruction accuracy was considered sufficient for many

beam diagnostic purposes and, subsequently, an experimental tomographic chamber (equipped with 12 observing ports) and set of 12 scanning cameras was constructed to assist with development tests of the prototype JET PINI neutral injector. The position of the viewing chamber with respect to the Culham Megawatt beam line and particle beam geometry is shown in Fig. 6.

4.1 Cameras

The cameras operate on the Flying-Spot Scanner principle described earlier[7]. However, instead of using the Fabry-Perot monochromator system to separate the Doppler-shifted emissions, a simpler method was used, based on incorporating a narrow-band 3-cavity Hα interference filter (FWHM ≐ 6 Å) in the optical path of each camera. By choosing the centre wavelength (λ6538 Å) of the filter to be offset by $\Delta\lambda \simeq 25$Å from the Hα rest wavelength, each of the shifted lines was detected independently by viewing the beam at the discrete angles

$$\theta_i = \sin^{-1} \left\{ \frac{c\,\Delta\,\lambda}{\lambda_o} \left(\frac{m_i}{2E_b} \right)^{1/2} \right\} \qquad \ldots(10)$$

to its normal. Here m_i (=1, 2 or 3 amu) correspond to masses of the extracted H^+, H_2^+ and H_3^+ ions.

The cameras used here were compact modules employing stepping motor drives to i) vary the tilt angle, θ, of the scan plane with respect to the normal to beam axis (to discriminate between the Doppler-shift components) and ii) drive the 4-sided pyramidal rotating mirror at speeds of $\lesssim$ 1000 rpm. Because of the angular constraint (eq. 10), the whole 'fan' of lines to a camera was tilted with respect to the beam

axis. The detected particle beam radiation came therefore from a region of axial length $\ell \simeq R_b \sin \theta_i$, where R_b is the beam diameter; for typical values $R_b \simeq 25$ cm and $\theta_2 = 25^0$ (for $E_b = 60$ keV), we find $\ell \simeq$ 10 cm. For cameras placed at $z = 7.6$m from the neutral beam source one expects a beam from a point source to have expanded by $\simeq 1\%$ of its radius in this observation distance. Since an expansion factor of this size is of the same order as the design reconstruction accuracy, it has been neglected here. Thus the assumption that the beam shape does not vary significantly in the axial direction (but mainly in the radial direction) is consistent with the design limit.

4.2 Overall System

A schematic diagram of the practical system is shown in Fig. 7. Because the Hα radiation was scanned in time, knowledge of the pointing angle, $\phi(t)$, of each camera was required in the data analysis in order to match the data to the elements in matrix O_{jk}. Each camera was synchronised with respect to a 'master' camera which also enabled its fiducial pointing angle ($\phi_0 = 0^0$) to be determined. Synchronisation was achieved electronically by using one pulse generator to actuate the 12 camera stepping motor drives via a corresponding set of motor power amplifiers. Trials showed that a pair of camera mirrors could be rotated at speeds up to 1000 rpm for several hours continuously with no change in relative pointing angle greater than the measurement accuracy of 1^0 of mirror rotation. The absolute pointing direction of each camera mirror was determined using a slotted disc (attached to the mirror drive shaft) and an infra-red photodiode/ detector. With this system it was possible to check both the synchronisation and absolute pointing direction of the cameras during operation on the beamline.

The filtered Hα radiation entering a camera was detected using a photomultiplier tube giving time varying signals which were then amplified, digitised and stored in the Megawatt Beamline data acquisition computer. The data could then be transmitted to the mainframe computer for image reconstruction.

4.3 Inter-Camera Sensitivity Calibration

Because up to twelve cameras were used to measure the beam projections, it was anticipated that differences might occur in the relative sensitivities of the cameras. Such effects could arise from variations in relative mirror reflectivity and interference filter characteristics as well as differences in the photomultiplier tube efficiencies. Two corrections for these effects were applied in the data analysis as follows.

The first correction was based on a point-source emitter approximation of the light beam source. Approximation of the particle beam as an isotropic (point) source of light at the centre of the observation tank would lead to equal photon fluxes arriving at each camera. Accordingly the total integrated intensity in each experimental set of projection data was equalised by multiplicative scaling thus eliminating any gross systematic errors and providing an initially calibrated data set. Higher order sensitivity corrections were then applied during iteration in the reconstruction analysis using a special feature of the ME method.

Firstly a ME reconstruction was calculated from the initially calibrated projection data. This solution was the most uniform, positive reconstruction consistent with the initially calibrated data. The non-

linear positivity constraint imposed by the entropy then allowed the retrieval of higher order systematic sensitivity correction factors in a way not possible using a linear reconstruction algorithm. The projections of the ME reconstruction were, at this stage, compared with the data using the χ^2 statistic. In general, it was found that this statistic was not fully optimised with respect to changes in the calibration factors for each of the cameras; by adjusting these it was then possible to optimise the χ^2 statistic making the re-corrected data more consistent with a positive reconstruction. Accordingly a new reconstruction was made, based on the re-corrected data, and a new set of correction factors generated. The correct calibration factors were thus determined iteratively using a simple binary chop. In practice, it was found that one or two re-calibrations was sufficient to optimise the value of χ^2 and the size of the corrections was $\lesssim$ 10%. Errors of inter-camera synchronisation can be corrected by a similar procedure.

5. RESULTS

Optical scans have been made on a hydrogen beam of constant energy (E_b = 60 keV) for various beam currents with the cameras tuned to receive optical Hα radiation from the full energy (θ = 19.0^0), radiation from the half energy (θ = 28.5^0), and one-third energy (θ = 35.0^0) particles. In each case the H_2 gas target thickness in the neutraliser was sufficiently large ($\int n_H \, d\ell \simeq 10^{16}$ cm^{-2}) to ensure nearly complete dissociation of the H_2^+ and H_3^+ ions. In these experiments, seven cameras were used (at positions C_1,C_2,C_3,C_4,C_6,C_8 and C_{12} in Fig. 3) to obtain projection data. The scan time was $\simeq$ 10 ms and data were sampled 1.5 s after the start of a 2 s beam pulse. Typically, a peak signal-to-noise ratio of 100 was obtained for the projection data.

Figures 8(a),(b) and (c) show contours of beam intensity derived from optical tomography for each of the energetic components E, E/2 and E/3 respectively. The beam energy (E = 60keV) and current (I_b = 34A) corresponded to the perveance matched condition. It is interesting to note the existence of a shallow 'cleavage' in the beam profile in Figs. 8(b) and (c). Such an effect is related to the construction of the accelerator grids in the source in which each half-source is steered and focussed independently, and a cleavage in the optical profile (at z $\leq$ 7.6m) has been observed previously[8]. Tomographic data were also obtained for source conditions in which the extracted beam current was lower than that required for the perveance matched condition (Fig. 9(a) and (b)). Here the beam envelope can be seen to have expanded compared with that observed under matched conditions (Fig. 8(a)). This expansion is consistent with the expected increase in beam divergence for $I_b \leq$ 34A (at constant E_b).

It will be useful to compare beam profile data from a number of different methods including water-flow calorimetry as well as optical Doppler-shift spectroscopy to attempt to obtain a self-consistent picture of beam transport. A detailed comparison of such data is beyond the scope of the present paper but will be described in a subsequent paper.

6. OTHER APPLICATIONS

Although the technique presented in this paper has been applied specifically to the problem of diagnosing an intense beam of particles, it can, in principle, be applied to many areas of high temperature plasma physics research in which suitable measurements of the plasma radiation can be obtained. Emitted soft X-rays can be collimated and

imaged on a linear array of detectors. For example, a rotating emissivity feature has been reconstructed on Alcator A tokamak[16] and similar experiments showing internal mode structures on JIPP-III stellarator[21, 22] have been performed using soft X-ray emissions. A theoretical investigation[23] of the use of ~ 10 (far infrared) interferometer lines of sight in the JET tokamak plasma has demonstrated the possibility of recovering 2D electron density information in the D-shaped plasma cross section. Tomographic application also exist in the field of plasma spectroscopy[24] where line-averaged spectral line data can be used to reconstruct the 2D volume emissivity function.

In most plasma containment devices, diagnostic access is usually restricted and it may only be possible to obtain data for a few projection angles, for such sparse data problems the possibility of using the ME technique is attractive in view of both the positivity constraint and ability to suppress noise on the reconstruction. Because the method is firmly based on information theory, the constrained maximisation of the image entropy introduces the least amount of artificial structure in the image.

ACKNOWLEDGEMENTS

It is a pleasure to acknowledge the operating team of the Culham Megawatt Beamline for assistance during the measurements. I also thank Drs. D.R. Sweetman, T.S. Green for advice and encouragement, C. Padgett M. Riviere and M. Magri-Overend for help in setting up the diagnostic system and M. Kemp, S.F. Gull and J. Skilling (MEDC) for discussions on sparse data reconstructions.

References

1. H. Altman et al., Proc. 11th Symp. on Fusion Tech. 2, 981-9 (1980).

2. I.D. Williams, J. Geddes, H.B. Gilbody, J. Phys. B: At. Mol. Phys. 15 (1982) 1377.

3. G.A. Cottrell, A.R. Martin, C. Padgett., Proc. 2nd Joint Grenoble-Varenna Int. Symp. on Heating in toroidal plasmas, Como, Italy (1980) Vol II, 945-951.

4. C.F. Burrell, W.S. Cooper, R.R. Smith and W.F. Sheele, Rev. Sci. Instrum., 51 (11), 1451-1462 (1980).

5. J.F. Bonnal, G. Bracco, C. Breton, C. de Michaelis, J. Druawx, M. Mattioli, R. Oberson and J. Ramette, J. Phys. D.: Appl. Phys., 15, 805-822 (1982).

6. J.F. Bonnal, C. Breton, C. de Michaelis, J. Druaux, M. Mattioli, R. Oberson and J. Ramette. Phys. Lett., 69A, 116-118 (1978).

7. G.A. Cottrell, J. Phys. E.: Sci. Instrum., 15, 91-96 (1982).

8. G.A. Cottrell, R. Hemsworth, M. Magri-Overend and C. Padgett, in preparation (1984).

9. T.S. Green, Proc. Int. Ion Engineering Conf., Vol I, 13-25. 12-16 September 1983. Kyoto Int. Conf. Hall. Sakyo-Ku, Kyoto, Japan. IEE Japan, Tokyo, Japan.

10. G.A. Cottrell, Rev. Sci. Instrum., 52 (8), 1174-1181 (1981).

11. Radon, J. Berichte Der Gesellschaft Der Wissenschaften Zu Leipzig, 69, 262 (1917).

12. R.N. Bracewell, Image Reconstruction from Projections (Topics in Applied Physics, Vol. 32); G.T. Herman ed., p81. Springer-Verlag, Berlin (1979).

13. D.J. de Rosier and A. Klug, Nature, 217, 130 (1968).

14. M. Kemp, Proc., IAEA/WHO Int. Symp. on Medical Radionuclide imaging. Heidelberg FRG. IAEA-SM-247/128 (1980).

15. G. Gilman and I. MacLeod, Computer Graphics Image Processing, 11, 227 (1979).

16. R.C. Chase, F.H. Seguin, M. Gerassimenko and R. Petrasso, Proc. S.P.I.E. Int. Optical Computing Conference, 231, 265 (1980).

17. C.E. Shannon and W. Weaver, The Mathematical Theory of Communication, Univ. of Illinois, Urbana, USA (1949).

18. S.W. Rowland, Image Reconstruction from Projections. Ed. G.T. Herman (Berlin: Springer-Verlag), 32, 9 (1979).

19. J. Skilling, Workshop on Maximum Entropy and Data Analysis. Laramie, Wyoming, USA (1981).

20. G.A. Cottrell, J. Phys. E: Sci. Instrum., 15, 432-438 (1982).

21. Y. Nagayama, S. Tsuji, K. Kawahata, N. Noda and S. Tanahashi. Jap. J. of Appl. Phys. 20, No 11. L779-L782 (1981).

22. S. Tsuji, Y. Nagayama, K. Kawahata, N. Noda and S. Tanahashi. Nuclear Fusion, 22, No 8, 1082-1085 (1982).

23. J.H. Williamson, D.E. Evans. Culham Laboratory Report CLM-P656 (1982).

24. B.R. Myers and M.A. Levine. Rev. Sci. Instrum, 49 (5), 610-616 (1978).

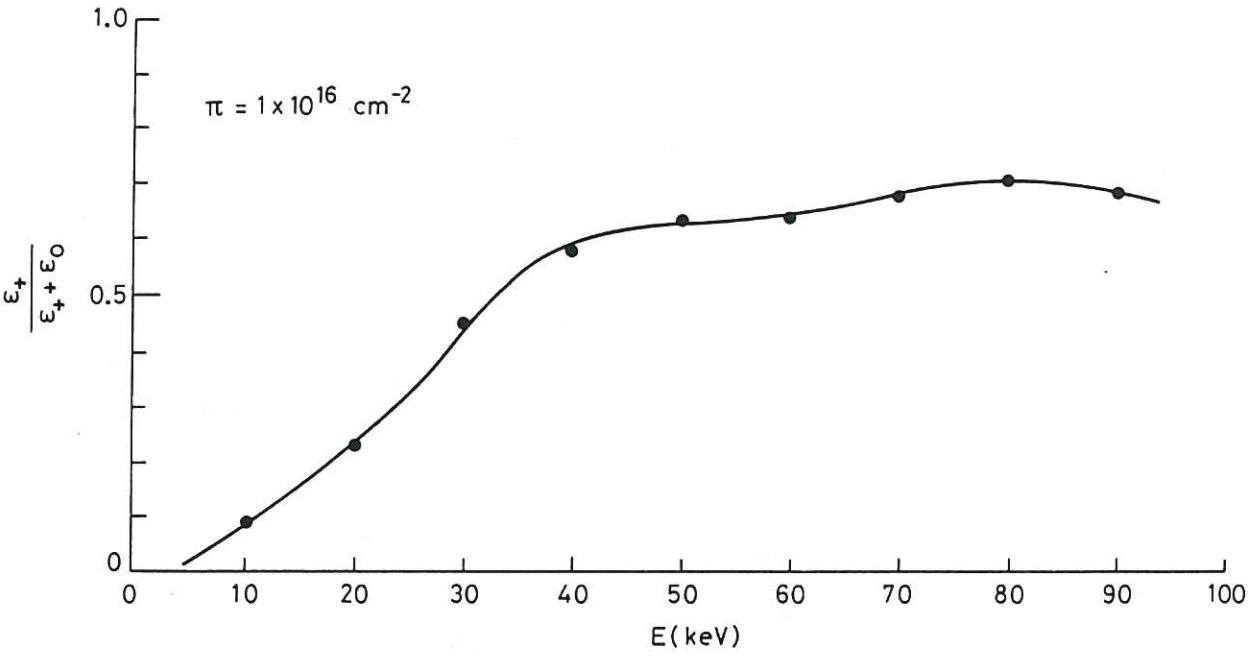

Fig.1 The fraction of the Hα emission per unit volume from ion charge-exchange reactions for a partially neutralised hydrogen beam of energy E.

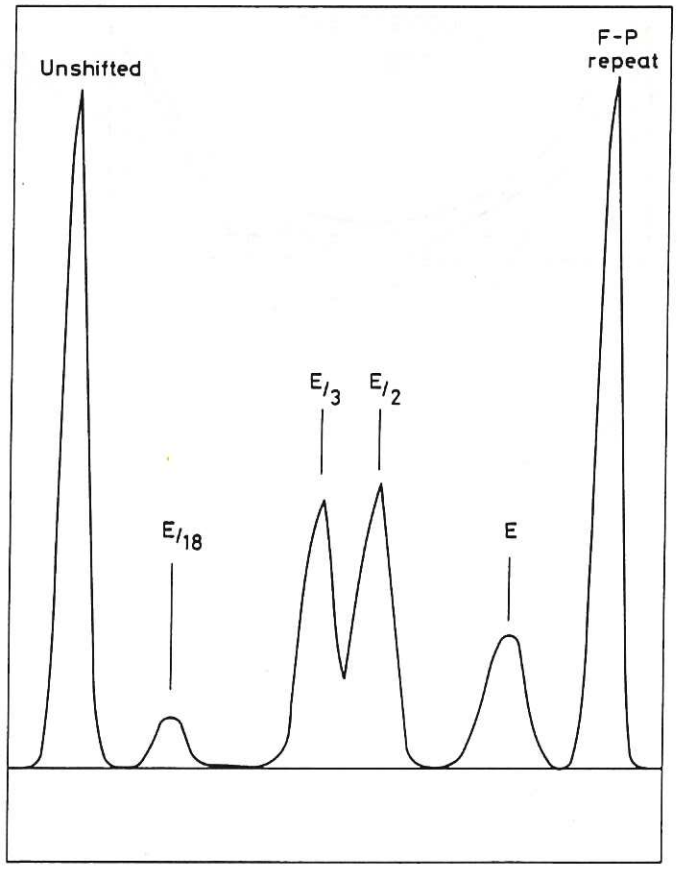

Fig.2 Doppler-shift spectrum of Hα radiation of a 75keV, 50A hydrogen beam obtained using a Fabry-Perot spectrometer on the Culham Megawatt beamline.

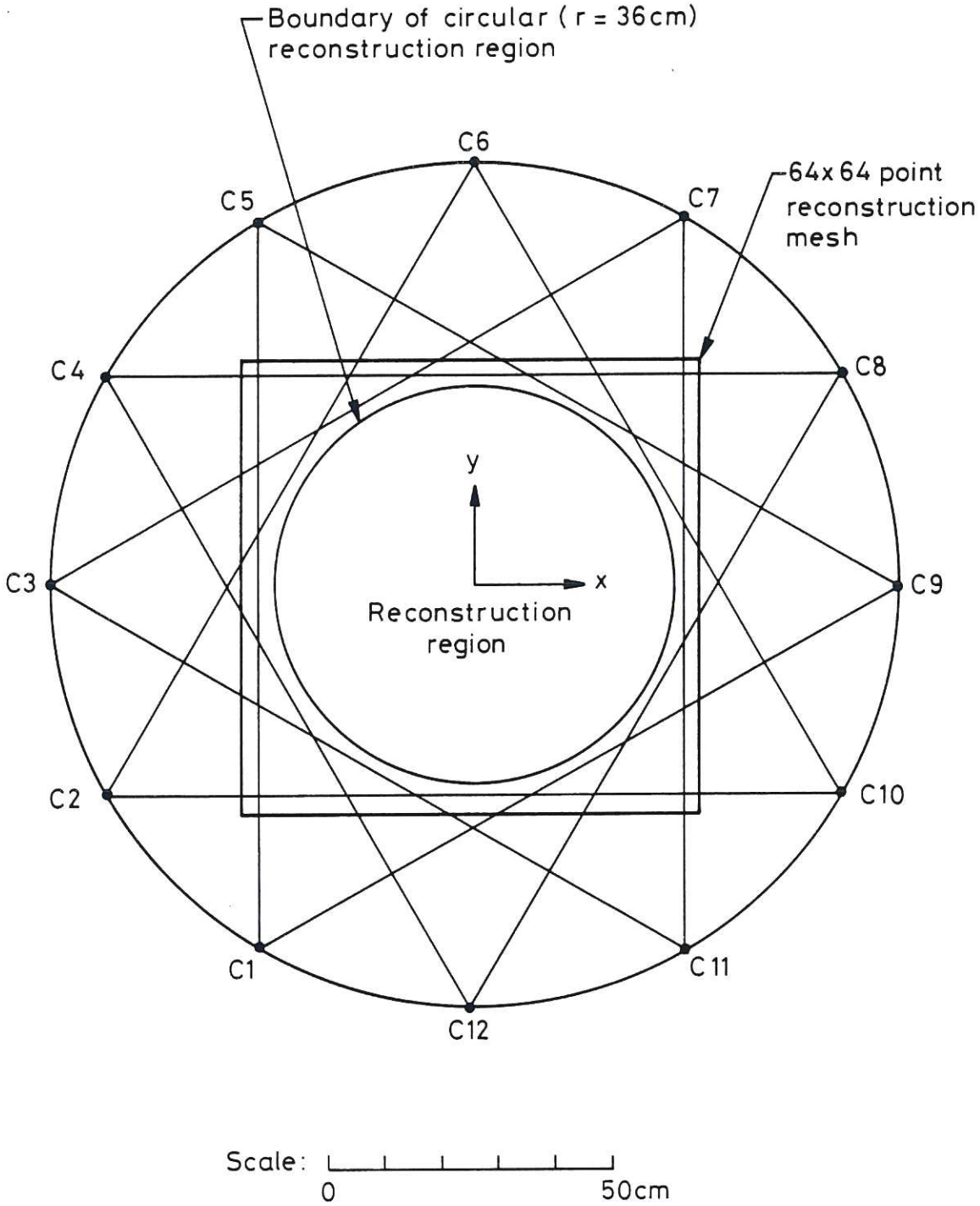

Fig.3 Geometry of scanner system projected onto a cross-section through the beamline. Camera stations are designated $C_1 - C_{12}$ and the lines of sight from each camera are the viewing limits. The inner circle is the reconstruction region lying within the (64 x 64 point) square reconstruction mesh. Each camera has a resolution of $\simeq 1^0$ giving $\simeq 60$ statistically independent lines of sight per camera. Thus there are a total of 720 lines of sight available to determine the object.

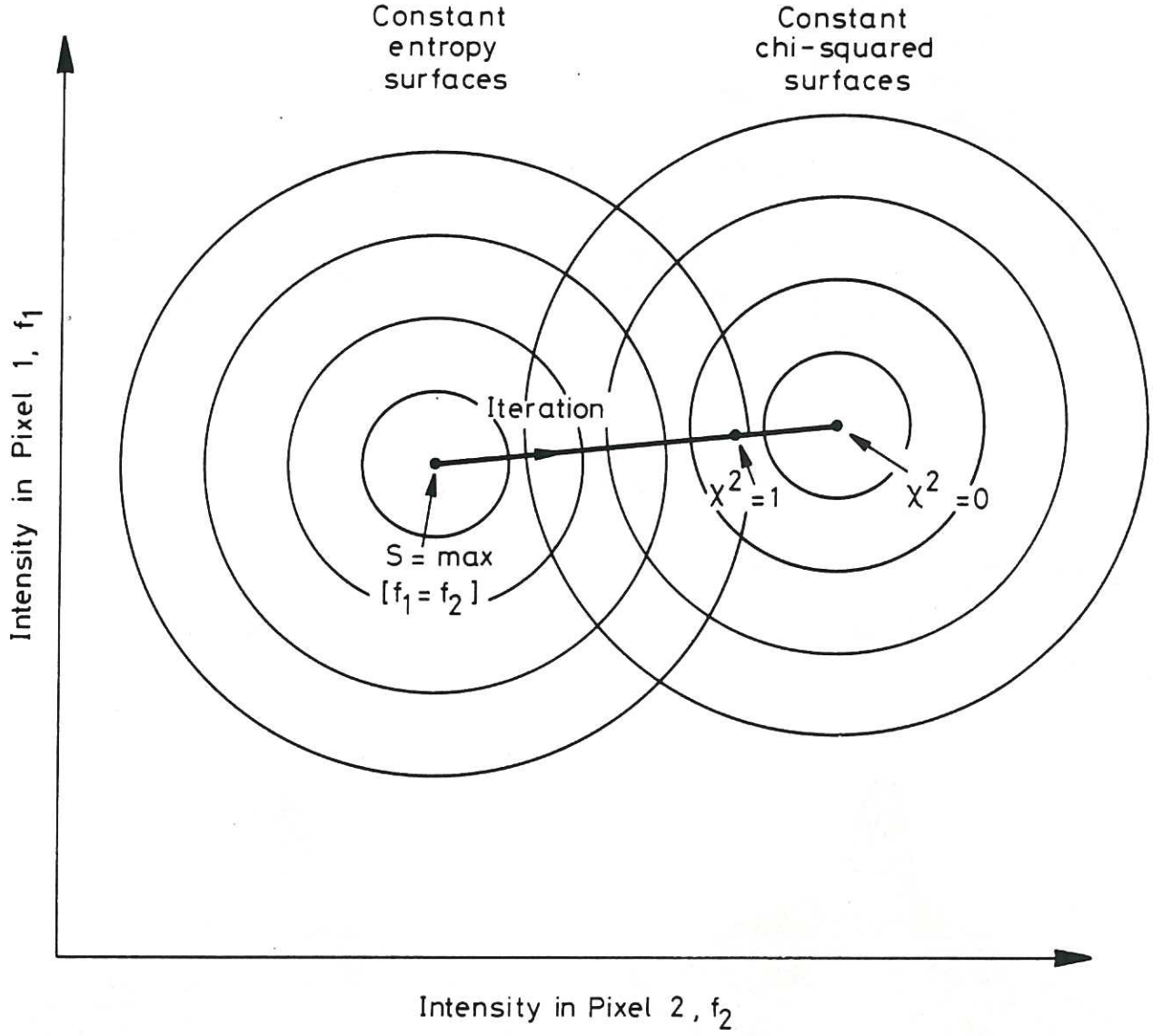

Fig.4 Two dimensional phase-space diagram showing start ($f_1 = f_2$) and end ($\chi^2 = 1$) points on the iteration path. See text for discussion. In the problem addressed here, the Maximum Entropy solution is found in a 4096-dimensional vector space.

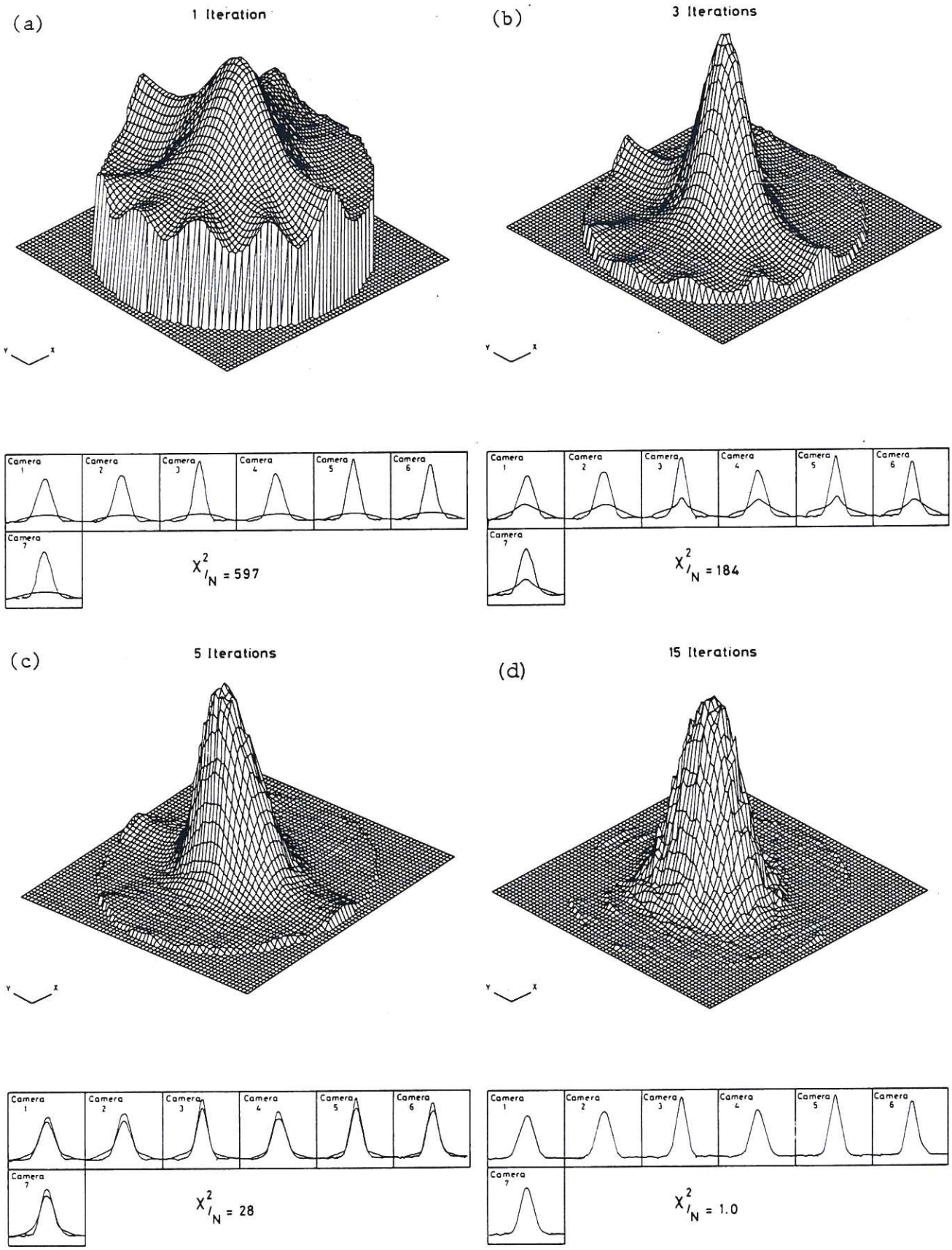

Fig.5 Development of the Maximum Entropy solution after (a) 1, (b) 3, (c) 5 and (d) 15 iterations shown in isometric projection. The camera projection data are shown below the solutions in each case; the upper of the two curves is the measured data, the lower the current projection of the (partially) optimised solution. After 15 iterations, the two sets of curves merge, showing that the data has been fitted by the algorithm, a condition defined by the value of normalised chi-squared reaching unity.

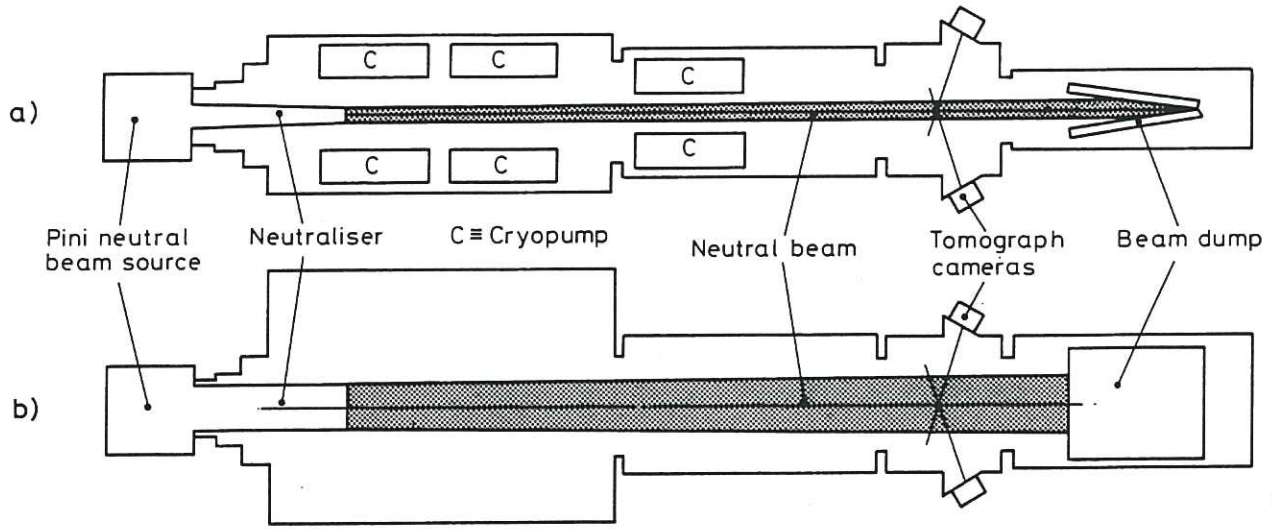

Fig.6 Experimental arrangement showing layout of vacuum tanks and tomography system on Culham Megawatt beamline. The distance between the PINI neutral beam source and the beam dump is approximately 10 metres.

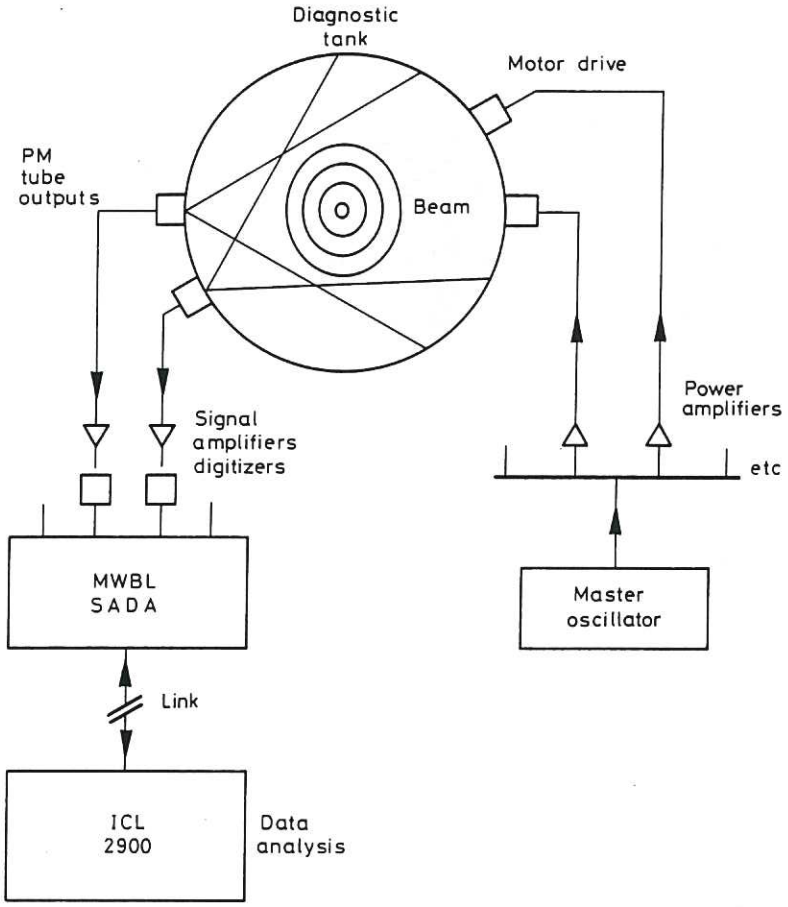

Detection and Scanning

Fig.7 Block diagram of the main components in the Neutral Beam Tomography system.

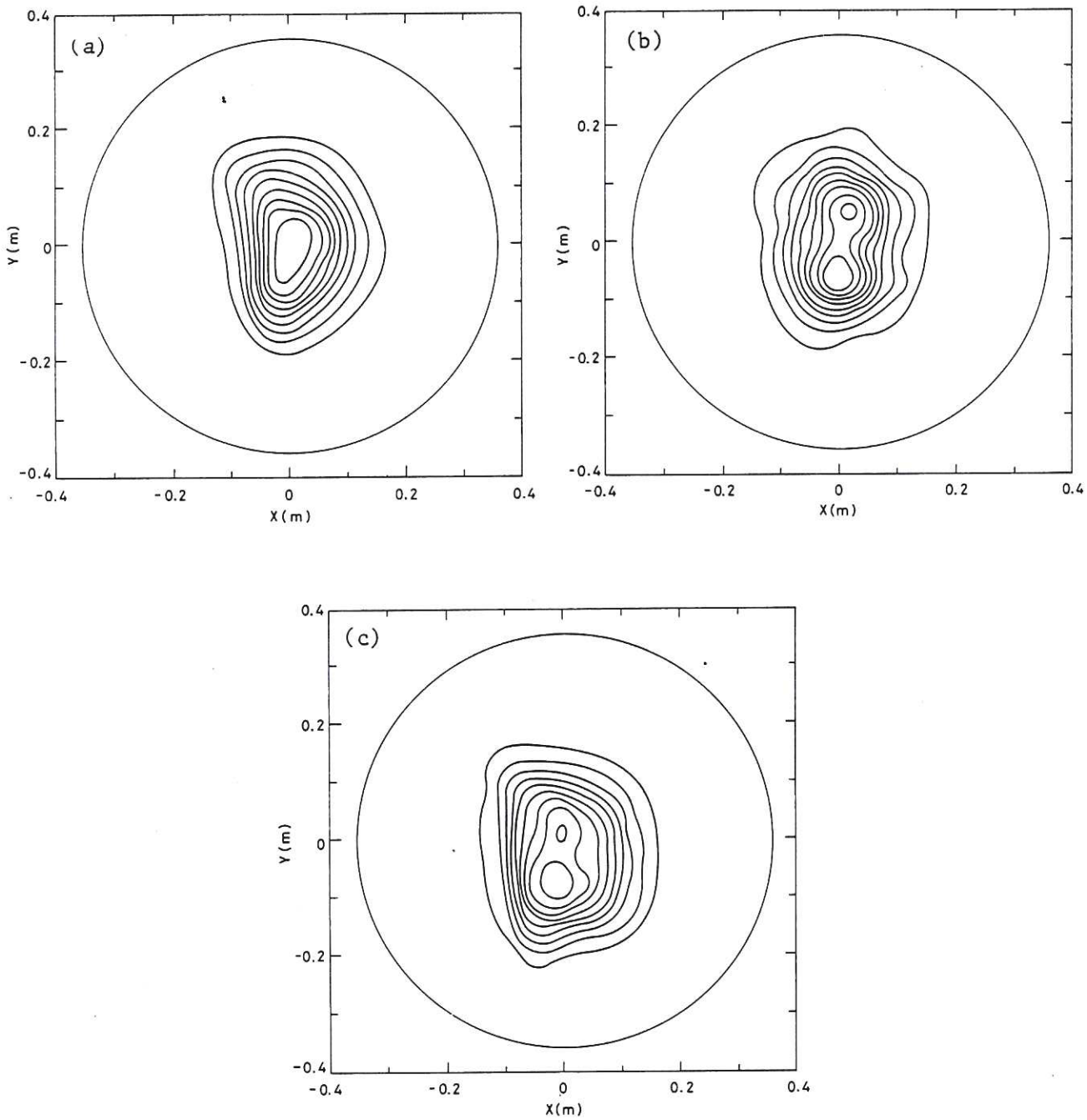

Fig.8 Tomographic reconstructions showing contours of optical intensity for (a) component with energy E, (b) component E/2 and (c) component E/3. Contour levels were normalised to the peak intensity and are at 10, 20, ..., 90% of the peak.

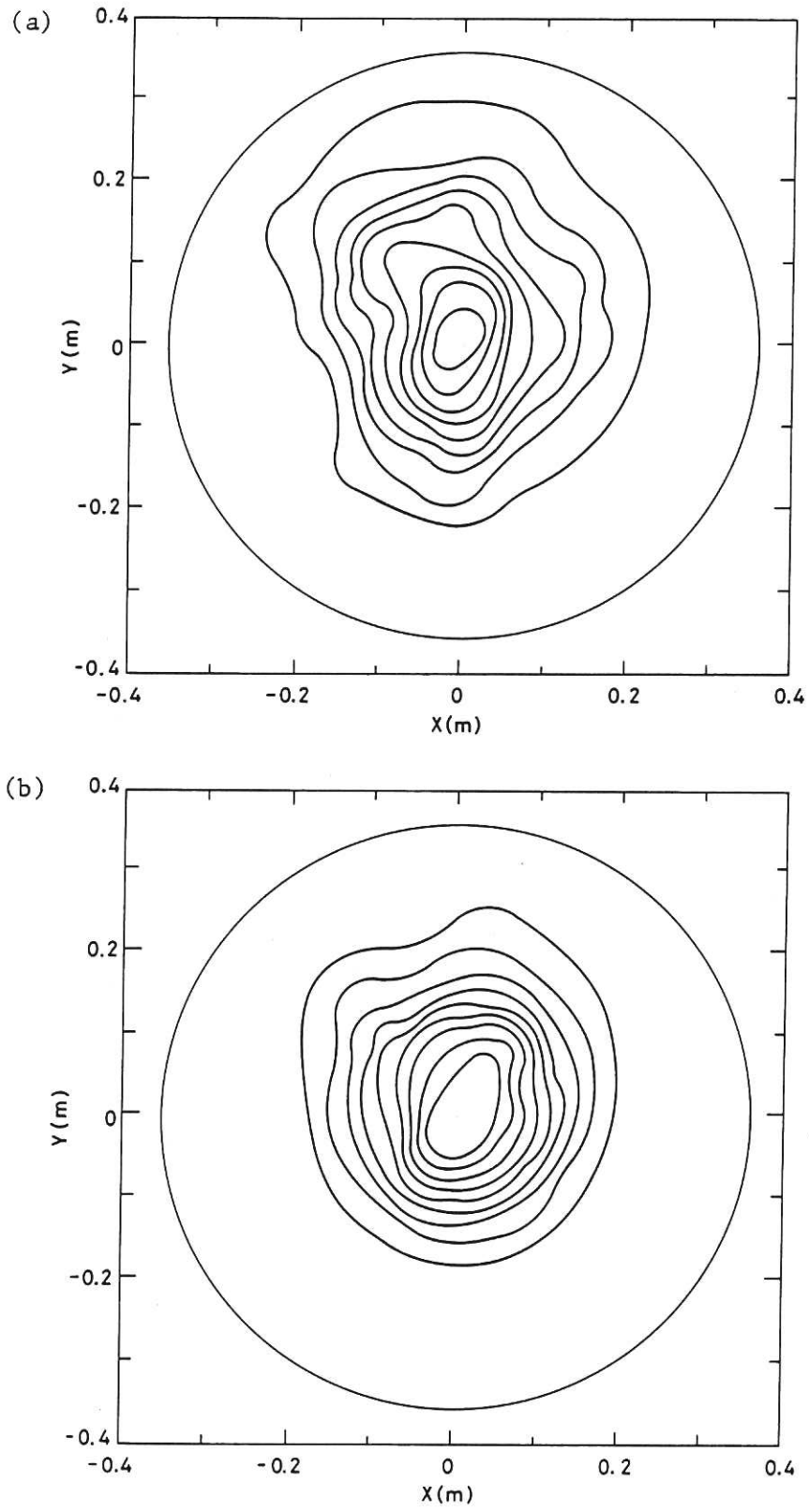

Fig.9 Tomographic reconstructions for full energy component but source operated below perveance-matched (I_b = 34A) condition (a) I_b = 29A; (b) I_b = 32A. Contour levels the same as in Fig.8.